Jiao et al. EURASIP Journal on Wireless Communications and Networking (2016) 2016:188
DOI 10.1186/s13638-016-0689-y

EURASIP Journal on Wireless Communications and Networking

RESEARCH Open Access

Monitoring fatigue cracks of a metal structure using an eddy current sensor

Shengbo Jiao[1*], Li Cheng[1,2], Xiaowei Li[3], Peiyuan Li[1] and Hua Ding[1]

Abstract

The present paper investigates monitoring of fatigue cracks of a metal structure using an eddy current micro sensor. Fatigue cracks tend to occur at bolt-jointed structures on an aircraft. In order to detect the damage quantitatively, a kind of change-prone micro eddy current sensor is designed and fabricated with flexible printed circuit board (FPCB) technology. A forward semi-analytical model is built by extracting a material's conductivity as the damage feature parameter, and characteristics analysis is conducted based on the model. The research focuses on setting up and utilizing the eddy current fields to analyze interaction of adjoining coils when the damage occurs, and investigating optimization on the working parameters of the sensor. In the experimental section, several common connection structures are applied to explore the sensor's monitoring ability both in air and in a corrosive environment. The result shows that the optimal working frequency is about 1 MHz. The eddy current micro sensor is capable of monitoring the crack growth with an accuracy of 1 mm, the average error being 4.6 % compared to fracture analysis. The sensor keeps high resolution of damage in aqueous corrosion. Due to the fretting fatigue, wear appears on the polyimide foil, leading to the decreases of the monitoring signal.

Keywords: Eddy current sensor, Smart washer, Crack monitoring, Metallic structure, Semi-analytical model

1 Introduction

Structure health monitoring (SHM) is the process of implementing a damage-identification strategy for civil infrastructures and mechanical parts [1]. Structural damage of an aircraft directly affects the safe reliability, mission availability, and service life of a military aircraft. At present, condition-based maintenance (CBM) is proposed as a promising philosophy for the application of accurate structural maintenance, instead of traditional scheduled maintenance based on various non-destructive technologies (NDT) [2]. Structure health monitoring could provide reliable information about the damage to a part that should be repaired or be replaced.

Extensive investigations have been presented and various sensors have been applied to monitor the state of structures in real time. Fiber Bragg grating (FBG) sensors have been extensively used as a powerful and highly effective method for structural health monitor [3–5], including soil nail system [6], slopes [7], piles [8, 9], and so on. The comparative vacuum monitoring (CVM), a process developed by the Structural Monitoring Systems (SMS) Company, has been used for monitoring on surface cracks in metallic structures. A series of 26 CVM sensors have been mounted on structure in four different DC-9, B-757, and B-767 aircrafts [10, 11]. Airbus has identified several SHM sensing systems used in their airplanes, including acoustic emission (AE), acousto-ultrasonic (AU) sensors, and eddy current foil sensors (ETFS). Giant magnetoresistive (GMR) sensor using uniform linear eddy current excitation and GMR field measurement has been developed to detect fatigue cracks around fasteners in multilayer structures [12, 13].

Eddy current non-destructive evaluation techniques have been widely used in the inspection of conduction structures for the detection of surface and near-surface cracks [14, 15]. The basic eddy current (EC) is a cylindrical coil used to generate and sense the electrical current in the metallic part simultaneously. Almeida et al. propose a new type of eddy current probe with enhanced lift-off immunity and improved sensitivity and estimates a new NDT system [16]. Vishnuvardhan et al. conduct structure health monitoring of anisotropic

* Correspondence: shengbojiao@sohu.com
[1]Aeronautic and Astronautic Engineering College, Air Force Engineering University, Xi'an 710038, China
Full list of author information is available at the end of the article

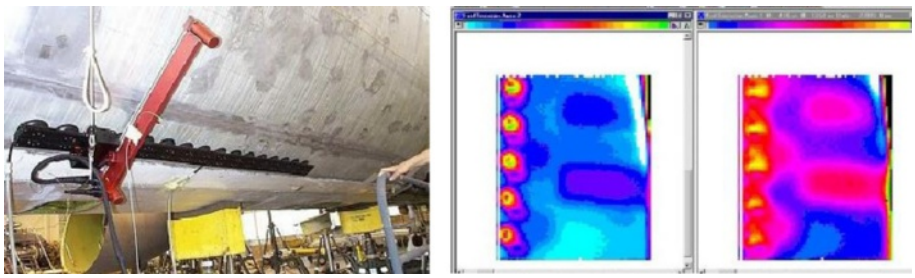

Fig. 1 TRECSCAN system. **a** TRECSCAN® probe. **b** TRECSCAN® imaging

plates with single-transmitter multiple-receiver (STMR) eddy current sensor array [17]. Goldfine et al. use permanently mounted meandering winding magnetometer (MWM) sensor arrays (MWM-arrays) with model-based multivariate inversion methods to detect crack initiation and monitor crack growth, which have been used in fatigue test of coupons and component as well as full-scale fatigue test [18–20].

Smith and Hugo have designed transient eddy currents and set up the TRECSCAN® system, which comprises a probe, an instrument, and a computer with the TRECSCAN software library linked to a scanning application such as ANDSCAN® or MAUS®, as shown in Fig. 1. They also developed new analytical methods allowing the compression of the wide dynamic range required so as to simultaneously view cracks in structures of widely different thicknesses in the same image [21–25]. Xu et al. [26–28] implement the senseless sensing method for process web sensors data.

However, the sensors mentioned above are commonly used to monitor the damage in position with no compress loading or evidence of fretting phenomenon. The primary structure of an aircraft is prone to fatigue damage. When a crack-sensitive sensor is mounted in a critical bolt-jointed metallic structure of aircraft to monitor cracking, the sensor is subjected to huge loading transferred by the bolt, which may significantly increase the risk of sensor failure. Although the array sensor like MWM and MWM-array can detect 50-μm long cracks, the available output signal is so tiny that it can hardly be detected. It is a hot topic of research to enhance the available output signal.

Taking into account the aggressive working conditions while monitoring crack damage located at a bolt-jointed area, the paper proposes a kind of grating eddy current macro displacement sensor as well as a smart washer designed to protect the transducer. By making the change of conductivity of the material equivalent to the structural damage feature, a damage monitoring semi-analytical model is built and distributions of the eddy current field and electromagnetic field are explored. A series of experiment are carried out to investigate the sensor's performance.

2 Grating eddy current micro displacement sensor

The circular sensor consists of multi-layered flexible coils. The arrayed excitation coils and measuring system—a plurality of induction coils located on both sides of the excitation coil—are arranged on different polyimide foils. While the sensor monitors the crack located on the critical bolt-jointed metallic structure, the sensor is subjected to huge loading. So a washer made of stainless steel is applied to protect the sensor. The schematic of the sensor and the washer are shown in Fig. 2.

The thickness of the foils is 0.0254 mm, and the coils sized 0.036 mm × 0.1016 mm (W × H) are array arranged with a 0.15-mm interval. The distance between the center of the hole and the first driving coil is 5 mm. A schematic

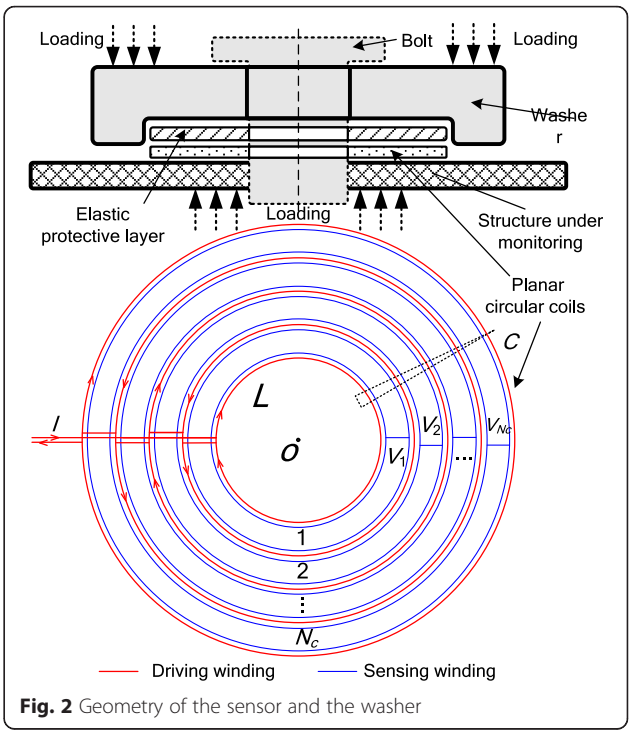

Fig. 2 Geometry of the sensor and the washer

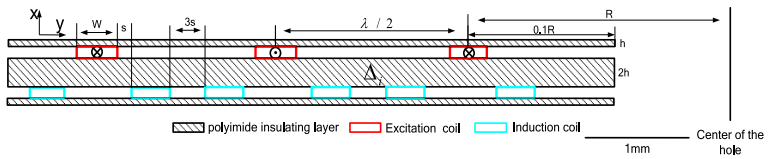

Fig. 3 Schematic diagram of eddy-current transducer (cross section)

cross-sectional view of the sensor is shown in Fig. 3. In Fig. 4, the sensor is attached on the pad by the polysulfide sealant HM-109 [29]. The load is transferred by the washer to protect the sensor from fretting damage.

The propagation of a flaw or crack in conductive specimens can be monitored by measuring the changes in magnetic fields. When measuring the magnetic field in eddy current testing, there are two magnetic fields present, which are superimposed. The first is the incident magnetic field from the excitation and the second is the reaction field. As the high-frequency alternating current flows though the excitation coil, primary magnetic field is produced around the space and an eddy current is induced in the structure. The induced magnetic field is also generated around the space. The distribution and intensity of the reflection field contains the information of structural state. The eddy current distribution in a metal is disturbed when the flaw initiates or the damage is enlarged. A schematic diagram of monitoring is displayed in Fig. 5.

3 Design of smart washer

There are a large number of bolt connection structures in an aircraft body, which are easy to fatigue fracture under vibration loads. How to use the eddy current sensor to monitor the state of the bolted connection structure becomes a difficult problem. Due to high pressure and fretting fatigue damage, which makes the sensor not work normally, a kind of protective device needs to design. To improve the eddy current sensor bearing capacity and to increase its durability, a specialized support pad—SmartWasher—was designed, as shown in Fig. 6. One side of the gasket is carved out of the same shape as the sensor, the depth of the groove of 0.3 mm, so that the sensor can be placed inside the groove to protect it; the sensor installation schematic is shown in Fig. 6.

To choose the appropriate material of the washer, fatigue monitor experiment was carried out with a different washer, which is made of stainless steel and aluminum. According to the sampling period and the loading frequency, noise reduction was conducted on the original data and signal amplitude of the output with the fatigue cycle number is shown in Fig. 7.

The inflection point is regarded as the feature points that the crack begin to propagate in Fig. 7. Point A of the first channel is the cumulative damage initiation point, and points B, C, and D of the second, third, and fourth induction channels correspond to the crack length 1, 2, and 3 mm, respectively. From the curve of Fig. 7, due to the larger conductivity of aluminum materials compared to stainless steel, a more strong eddy current field is generated on the surface of the gasket, leading to lower noise ratio, and then the curve is not smooth enough.

Then the static analysis of the washer was conducted with ANSYS. The finite element model of the sensor and the supporting pad was established by using the Solid45 element, as shown in Fig. 8. Using this model, the stress and deformation of the sensor and the supporting pad under compression force were analyzed, as shown in Fig. 9. The maximum stress in gasket locates at the inner edge of the groove, and maximum deformation appears at the edge of the hole. As to the sensor, maximum stress and deformation both occur at the edge of the hole.

The finite element model is then used to analyze the maximum stress and deformation of the sensor when the normalized radius of the support pad is increased from 0.5 to 0.85, as shown in Fig. 10. It can be seen that with the increase of the radius of the gasket, the maximum von Mises stress and maximum deformation of the sensor will be reduced slowly. When the normalized radius of the gasket is increased from 0.5 to 0.85, the maximum stress is only less than 0.1 MPa, and the deformation is only 0.01 μm.

Fig. 4 Grating eddy current micro displacement sensor and smart washer

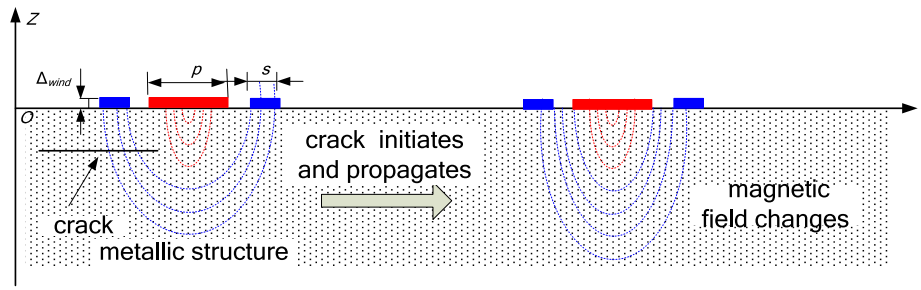

Fig. 5 Magnetic field is disturbed as the crack initiates and propagates (schematic diagram)

4 Forward semi-analytical equivalent model

The key point of modeling in structure health monitoring is to build the relationships between the structure damage features and the output signal. Generally, researches can be divided into two categories: forward models and reverse models. The forward models lay foundation for the reverse ones, and the former models are more convenient in conducting further study on the output signal from the mechanism. Also, the forward models are helpful in optimizing the sensor's parameters and construction of an inversion model [30–32].

In this paper, the electromagnetic parameters of materials are equivalent to the structural damage features [33], and the damage monitoring semi-analytical model of the attached eddy current sensor is established. The model demonstrates the relationship between the output signal and the excitation frequency, sensor's parameters, as well as the electromagnetic parameters of the structure to be monitored. Since the building of the model is dramatically complicated and cumbersome, in this section modeling process is described briefly and shown in Fig. 11. Some of the specific modeling process used here can be understood with the help of reference [34].

The sensor is placed on the top of the monitored structure. The lift-off distance is ΔL and the thickness of the structure is ΔS. The conductivity is σ and the permeability is μ. The widths of the excitation coil and of the induction coil are p and s, respectively. The length between the two coils is g and the coil thickness is Δ_{wind}. The spacing length λ between the adjacent excitation coils is defined as the wavelength of the sensor. The general solution of the differential equations of time-harmonic field function A under cylindrical coordinates can be expressed in the following form:

$$\mathbf{A} = J_1(kr)(c_1 e^{\chi z} + c_2 e^{-\chi z})\overrightarrow{\varphi}. \tag{1}$$

Here, $\chi^2 = k^2 + j\omega\mu\sigma$, ω is the excitation frequency, σ is the conductivity of dielectric polyimide layer, μ is the permeability of the layer, and k is a constant. J_1 is a first-order Bessel function of the first type. At the cross section $Z = 0$, a Bessel function expression of current density K and magnetic vector A is obtained from Eq. (1) [35].

$$K(r) = \sum_{n=1}^{\infty} K_{Bn} J_1\left(\frac{\alpha_n}{R} r\right) \tag{2}$$

$$A(r) = \sum_{n=1}^{\infty} A_{Bn} J_1\left(\frac{\alpha_n}{R} r\right) \tag{3}$$

In the two equations above, α_n is the forward zero sequence of J_1, and R is the outer boundary of the model. Discrete allocation points and sub-domains are configured at the coil cross section, which is shown in Fig. 12. Regarding the current density of discrete points as unknown parameters, the vector expression of K_{Bn}, which is the coefficient of K, will be obtained by the series formula of Bessel function according to the linear

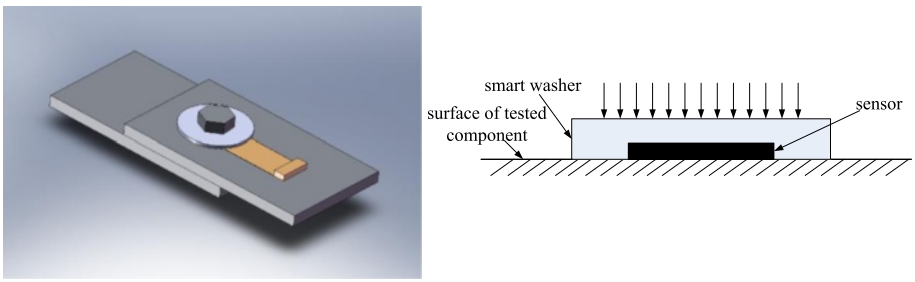

Fig. 6 Diagram of smart washer

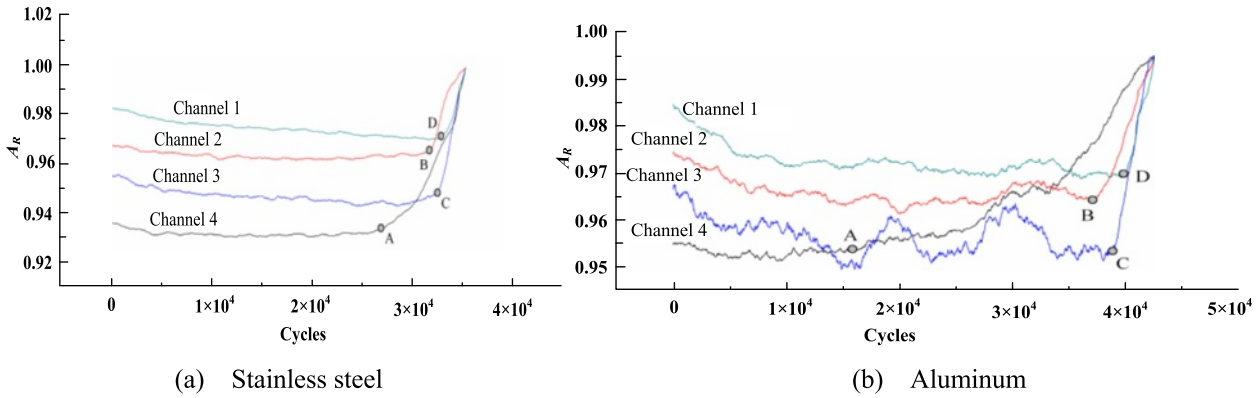

Fig. 7 Change curve of amplitude ratio signal with load frequency. **a** Stainless steel. **b** Aluminum

distribution assumption of current between the adjacent discrete points.

$$K_{Bn} = \mathbf{MK} \tag{4}$$

K is a vector composed of the unknown current density at all discrete points, and M is the coefficient matrix. The current density of the coil is calculated at the cross section as Eq. (4) and is substituted into Eq. (2). Meanwhile, according to the field relations at the interface between the media layer, as well as the boundaries conditions at the cross section of coils, the expression of the vector A_{Bn} is taken, which is the coefficient of the magnetic vector A.

$$A_{Bn} = TK_{Bn} \tag{5}$$

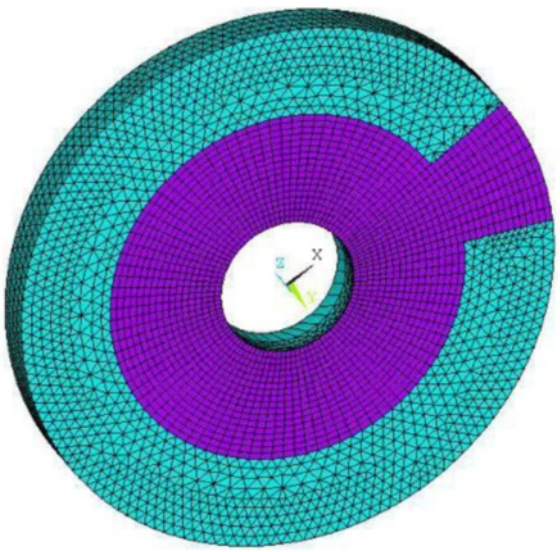

Fig. 8 Finite element model

Then the magnetic vector A is obtained by substituting Eq. (5) into Eq. (3). Applying Faraday's law of electromagnetic induction to every closed path, we can obtain:

$$v = j\omega(2\pi r')A_{\varphi}(r') + 2\pi r' \frac{K(r')}{\Delta_{\text{wind}}\sigma_{\text{wind}}}, \tag{6}$$

where v is the voltage source, that is, the input to the excitation coil and output from the induction coil. Δ_{wind} is the thickness of the coil, and σ_{wind} is the conductivity of the conductor. Each side of Eq. (6) is integrated at the defined sub-region, and the following expression is obtained:

$$\mathbf{M}_{TU}\mathbf{K} = \mathbf{V} \tag{7}$$

In Eq. (7), V is the vector of the voltage source, and subscript T is the index of sub-region. Considering the constraint relations between the current density and current in the excitation coil as well as the induction coil, the following matrix expression is established:

$$\mathbf{M}_{TD}\mathbf{K} = \mathbf{I} \tag{8}$$

Uniting Eqs. (7) and (8), we can obtain the matrix equation involving the unknown line current density and voltage induction coil in all discrete points. The excitation coil current is defined as 1 A, according to the theory of linear equations we can obtain the induced voltage of every channel's induction coil, as well as the induction coil resistance value across the channel.

$$\begin{bmatrix} \mathbf{M}_{TU} & \mathbf{M}_{TL} \\ \mathbf{M}_{TD} & 0 \end{bmatrix} \begin{bmatrix} \mathbf{K} \\ \mathbf{V} \end{bmatrix} = \begin{bmatrix} \mathbf{0} \\ \mathbf{I} \end{bmatrix} \tag{9}$$

5 Sensor's trans-impedance response and optimization

5.1 Analysis of trans-impedance response

The sensitivity of the sensor reflects the changing amplitude of output signal as the crack extends by 1 mm in the structure. For the established equivalent model, it is

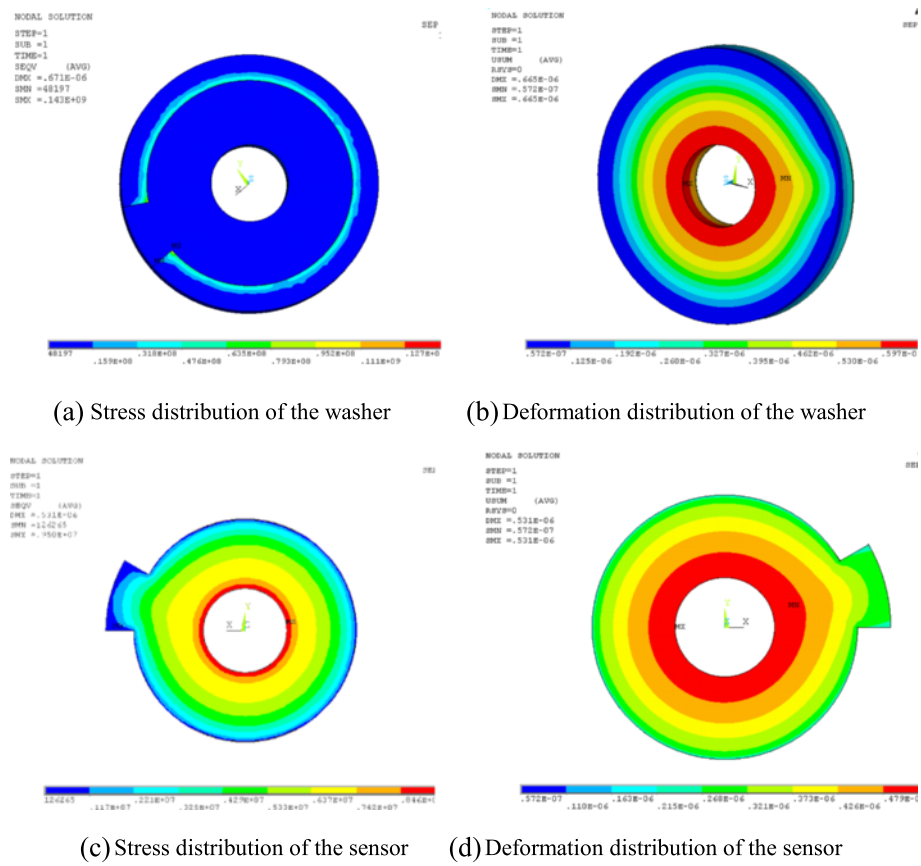

Fig. 9 Results of finite element analysis. **a** Stress distribution of the washer. **b** Deformation distribution of the washer. **c** Stress distribution of the sensor. **d** Deformation distribution of the sensor

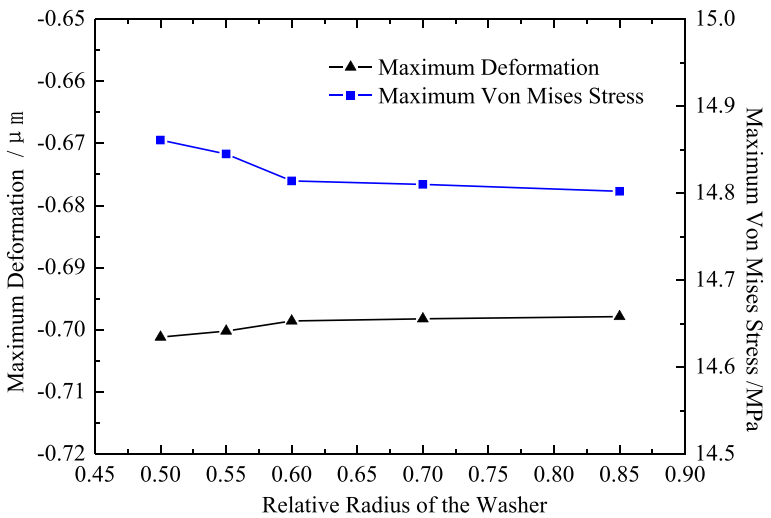

Fig. 10 The maximum stress and deformation with the radius of the washer

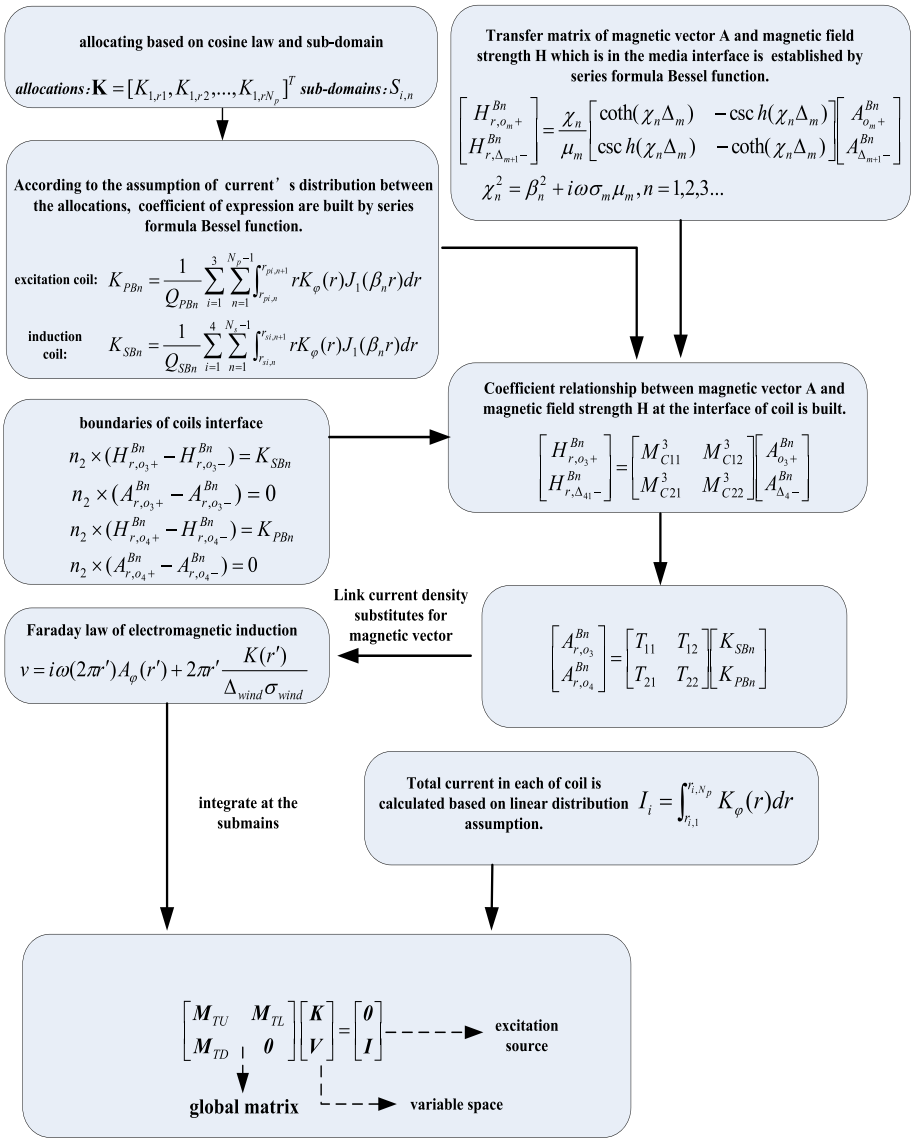

Fig. 11 Forward semi-analytical modeling route of the sensor

the sensitivity to the conductivity of material. The expression of sensitivity is defined as follows:

$$S_\sigma=\sqrt{\left(\frac{\partial Z_A}{\partial\sigma}\right)^2+\left(\frac{\partial Z_\Phi}{\partial\sigma}\right)^2}, \tag{10}$$

where S_σ is the sensitivity and Z_A is the amplitude of the output signal, while Z_Φ is the phase. Lift-off defined to be the distance between the sensor and the tested structure, has put a major impact on the distribution of eddy current and of electromagnetic field. In order to

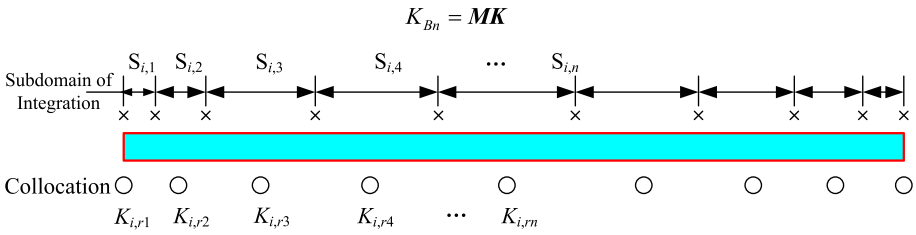

Fig. 12 Allocation and sub-domain in *i*th driving winding cross section

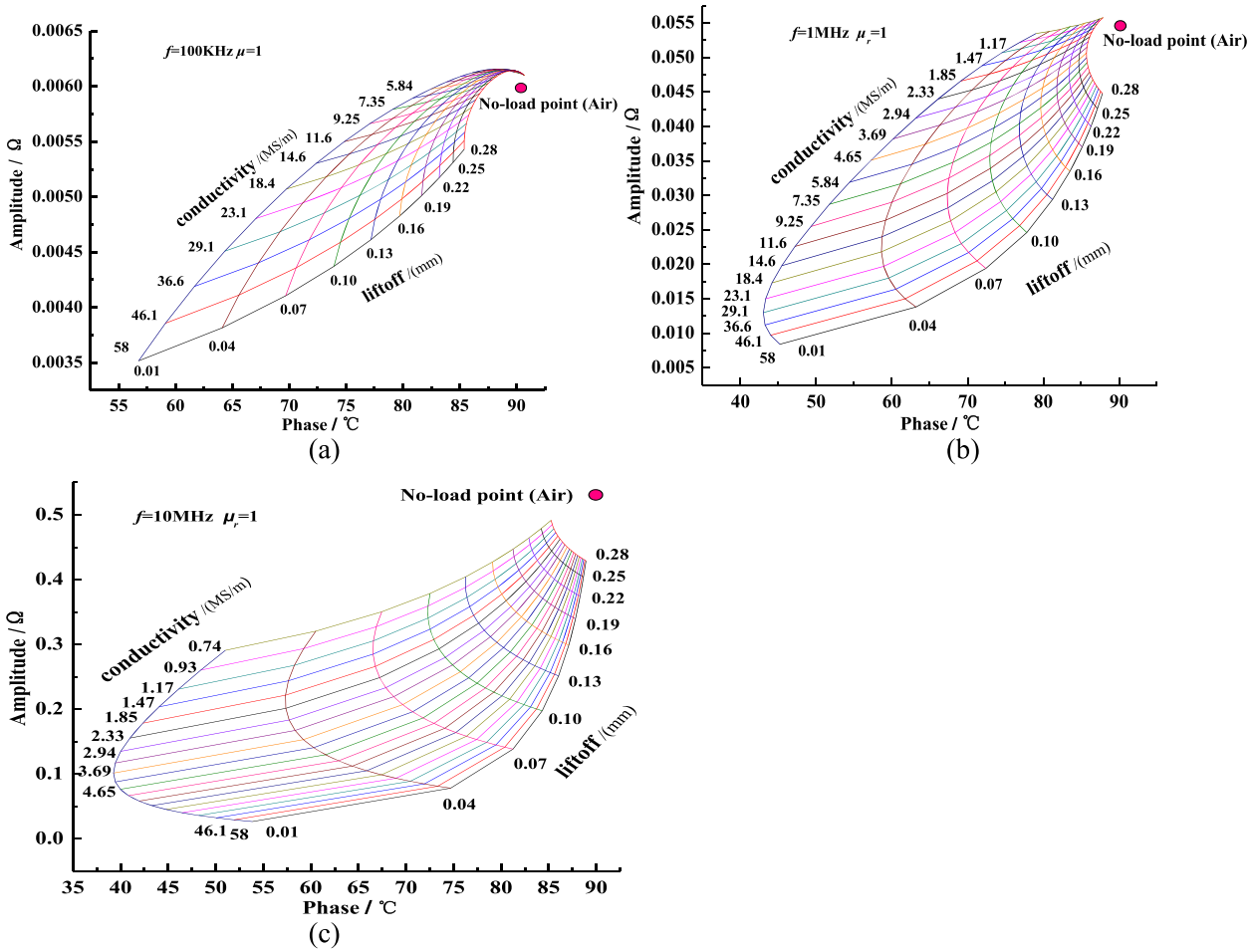

Fig. 13 Double parameter grid diagram of sensor trans-impedance. **a** 100 KHz. **b** 1 MHz. **c** 10 MHz

convey clearly the trans-impedance output along with the input parameters such as electrical conductivity and lift-off distance, the paper utilizes a method of grids plane to display the relationship intuitively. Figure 13 shows the dual parameter grid planes. The frequencies are 100 KHz, 1 MHz, and 10 MHz, respectively. In Fig. 13, the lift-off is uniformly spaced, from 0.01 to 0.28 mm, with an interval of 0.03 mm. Conductivity changes proportionally with ratio coefficients of 0.795 and 0.64, respectively. Conductivity ranges from 58 to 0.74 MS/m.

As the lift-off increases, the trans-impedance grids are all contracting towards the load point which represents the sensor's output in the air, and the size of grid cells becomes smaller constantly. That is, the sensitivity of the sensor is decreasing as the lift-off lengthens. At the frequency of 100 KHz and 10 MHz, as the conductivity gets higher, the sensitivity increases. While at the

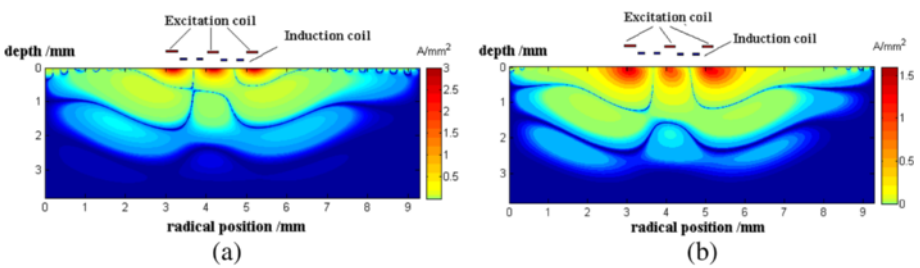

Fig. 14 Eddy current field distribution in the monitored structure. **a** $\omega t = 0$, $f = 1$ MHz. **b** $\omega t = \pi/2$, $f = 1$ MHz

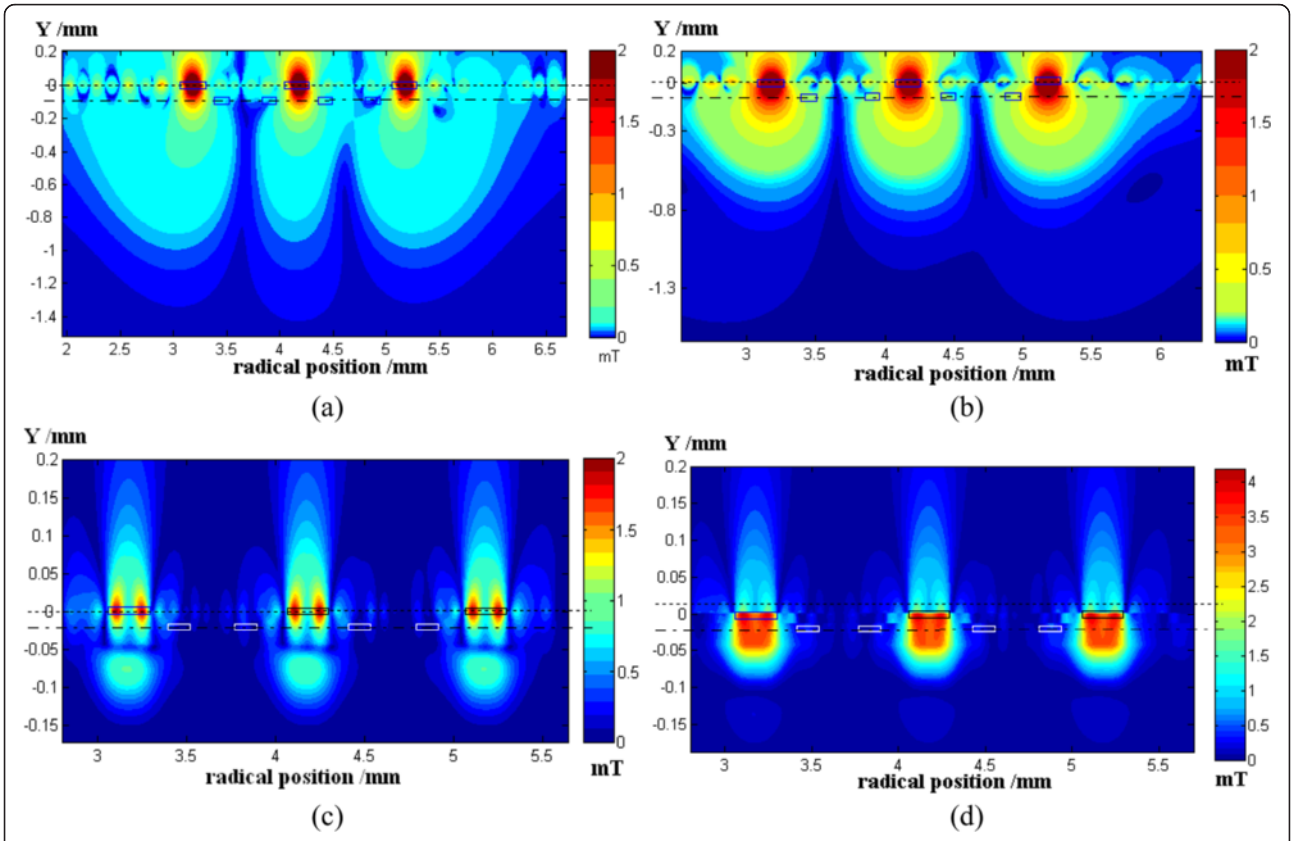

Fig. 15 Distribution of space magnetic induction. **a** $\omega t = 0$, $f = 1$ MHz. **b** $\omega t = \pi/2$, $f = 1$ MHz. **c** $\omega t = 0$, $f = 10$ MHz. **d** $\omega t = \pi/2$, $f = 10$ MHz

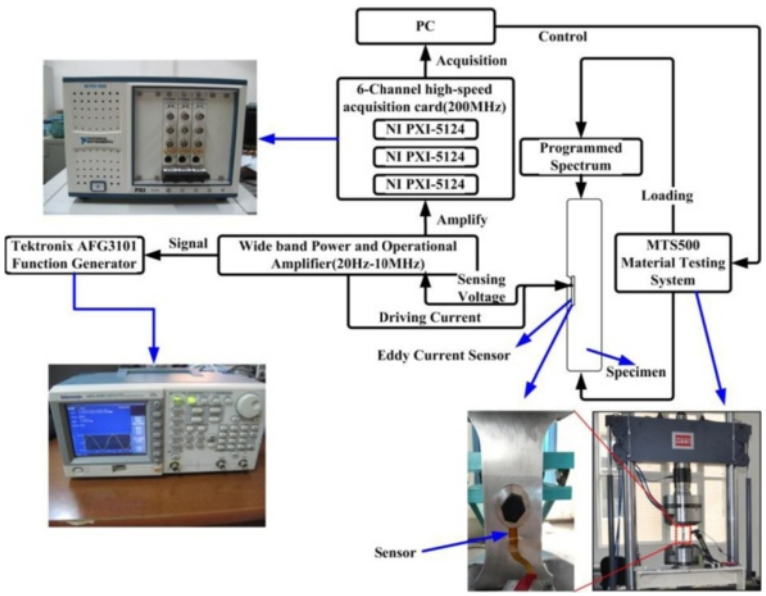

Fig. 16 Experiment setup

Table 1 Features of experiment setup

Parameters	Description
Signal generator	f = 0.1 Hz–10 MHz, four channels
AC amplifier	10–50 dB, nominal power 15 W, optional pre-amp
Acquisition card	6 channels, up to 200 MHz sampling rate
Input	4 real-time inputs, 8 control, inputs, external trigger, external gate
Output	Real-time multiplexed controller, 8, programmable control outputs

frequency of 1 MHz, the sensitivity is largest in the middle range of conductivity. With the increase of frequency, the eddy current is concentrating on the surface of the structure which will reduce the capability of monitoring the deep crack in the structure. So the optimal frequency is about 1 MHz.

5.2 Spatial distribution of eddy current field and magnetic field

According to the semi-analytical model, the distribution in the surrounding medium space of the magnetic field and the eddy current fields is explored at different excitation frequencies. This enhances the understanding of the output characteristics of the electromagnetic field. Due to the large amount of calculation, the number of induction coils in the simulation will be reduced to two channels.

In order to obtain the instantaneous distribution, the analysis is processed from two aspects separately: real part and imaginary part. That means one analyzes the form of the field distribution at the points of $\omega t = 0$ and $\omega t = \pi/2$ in a harmonic period. ($K = \sin(\omega t + \varphi)$, $\omega t = 0$, that corresponds to the imaginary part of the complex parameter, while $\omega t = \pi/2$ correspond to the real part of the complex parameter). The contour map of the eddy current field distribution in the cases of $\omega t = 0$ and $\omega t = \pi/2$ under the excitation frequency 1 MHz are shown in Fig. 14. The vertical axis depth 0 corresponds to the structure surface of 2A12-T4 aluminum alloy structure.

In Fig. 14, the eddy current field is concentrated beneath the sensor, and there are three vortex wave sources formed by excitation coils in the monitored structure. The three vortex wave sources diffuse and attenuate in the form of waves towards the inner and the edge of the structure. Meanwhile, due to the opposite direction of the excitation current among the excitation coils, there exist the zero points in the eddy current field, shown as the boundaries among the wave sources. The contour map of magnetic induction strength distribution is shown in Fig. 15, as the eddy current sensor is attached to the 2A12-T4 aluminum alloy surface.

Similarly, there are also three field sources which diffuse and attenuate in the form of waves towards the space. The skin effect in the distribution of the coil current density is more obvious at the frequency of 10 MHz, so the excitation source is concentrated around the two edges of the coil, so that each excitation coil contains two excitation points. There is a big difference in the magnetic induction intensity between $\omega t = 0$ and $\omega t = \pi/2$ at the frequency of 10 MHz. This may be due to the fact that at the frequency of 10 MHz, the eddy current field intensity is very large, and thus, the magnetic field has put a great effect on the spatial distribution of the excitation source magnetic field. At $\omega t = 0$, the excitation source magnetic field is weakened by the magnetic field generated by eddy current, while at $\omega t = \pi/2$, the excitation source magnetic field is amplified.

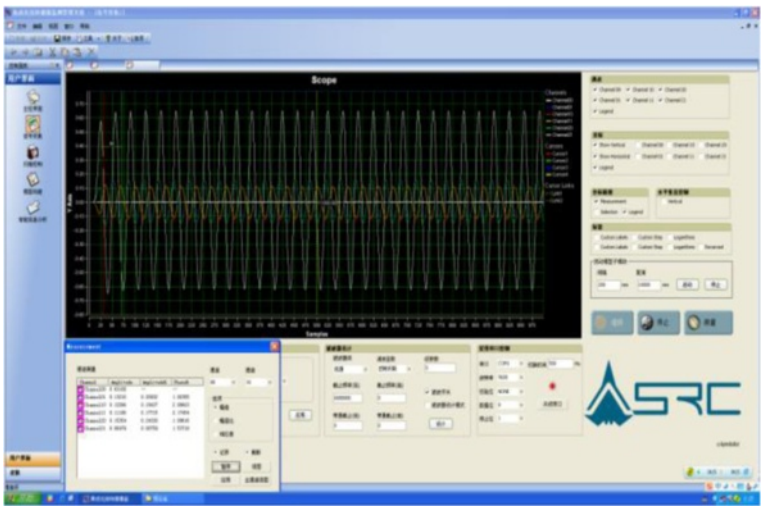

Fig. 17 The self-developed monitoring software

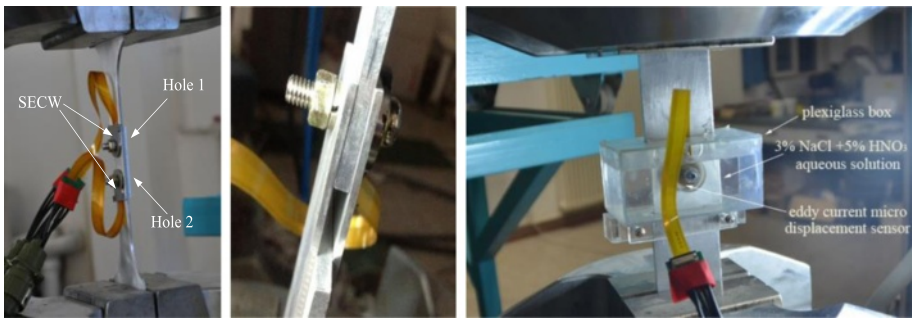

Fig. 18 Overlapping structure and corrosion fatigue test

6 Experiment setup

The experimental system is shown in Fig. 16. A driving signal is produced by the Tektronix AFG3101 function generator and amplified by the power amplifier before driving the coils. The seak voltage of four dependent sensing coils is amplified to improve SNR and collected, respectively, by a 6-channel high-speed acquisition card. The features are shown in Table 1. Using the MTS 500 material test system, programmed spectrums are applied to implement fatigue crack initiation and propagation. In order to detect the signal in real time, we developed the monitoring software shown in Fig. 17. The driving signal and the four inducing signal are displayed on the software interface. As the amplitude of the inducing signal approaches a certain value, the software will post warnings.

7 Experiment condition

The specimen is made of 2A12-T4 aluminum. As we know, bolt-jointed overlapping structures generally utilized in aircraft are considered as the critical fatigue crack position. Due to the coupling environment composed of load and corrosion during its service life, the components of the aircraft are surface treated by anticathode oxidation technology. Different types of structure and influence of aggressive environments should be investigated as well as effects of oxidation. So the experiment is divided into two groups. In the first group, the specimen is an overlapping structure; the sensor is embedded into the washer that is compressed between the two dumbbell-shaped sheets sized 250 mm × 50 mm × 2 mm by screw. In the second group, the experiment is tested in 3 % NaCl + 5 % HNO_3 aqueous solution as compared to the results tested in air. The specimen is shown in Fig. 18.

The fatigue damage monitoring experiment is carried out on an MTS 500 material test machine at room temperature. Constant amplitude loading is applied in this experiment. The experimental parameters are set as follows: loading frequency $f = 15$ Hz; stress ratio $R = 0.06$; maximum stress $\sigma_{max} = 200$ Mpa. The frequency of excitation signal is 1 MHz. Programmed loading spectrum is shown in Table 2. To guarantee the same liftoff in the experiments, use torque wrench to fix the screw.

Due to the stress concentration around the hole, the fatigue damage occurs on the middle part of the joint specimen, and the crack is shield by nut so direct measurement is not accessible. As a result, the experiment is not stopped until the specimen ruptured. During the experiment, the voltage values of the four dependent inducing coils are recorded along with the fatigue damage initiation and propagation.

8 Results and analysis

Taking into account the stress concentration, it can be learnt that the crack initiates from the edge of the hole under the constant cyclic load. In the first group, we put two sensors each on the top and bottom holes. As a result, after 4.3×10^4 cyclic load, the specimen eventually ruptures from the top section. Figure 19 gives the signal changes of the four sensing coils named channels 1 to 4. The curves maintain horizontal and stable initially. After 2.87×10^4 loads, the curve of the first channel signal begins to rise and the others climb in succession after a certain number of cyclic loads. This demonstrates that as the crack extends, the damage is detected gradually by the arrayed coils.

At key points A, B, C, and D, the sensing coil senses changes of the specimen, indicating the moment that the magnetic field of each coil is first disturbed by the crack. The radial distance of adjacent sensing coils is 1 mm, that is to say, the sensor has monitored the growth of crack with an accuracy of 1 mm. The crack growth rate increases with the crack extension with the

Table 2 Programmed load spectrum

	Stress level (MPa)	Ratio	Cycles
Low load	150	0.06	2500
High load	200	0.06	100

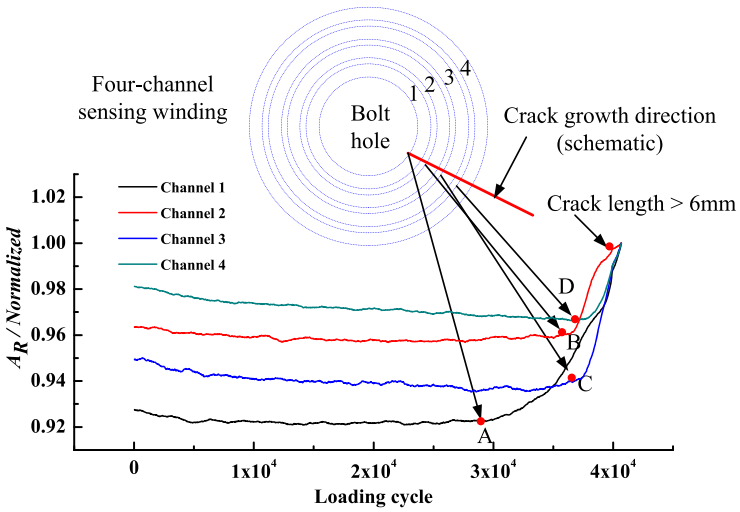

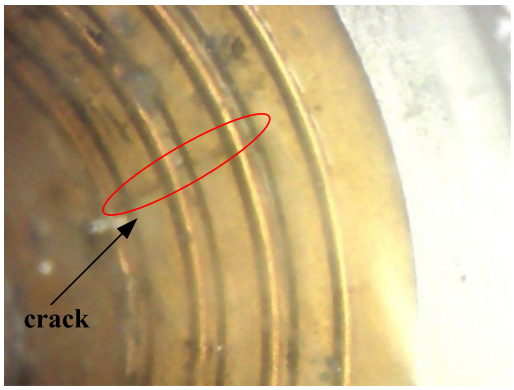

Fig. 19 Changes of the signal sampled by the sensor (top sensor)

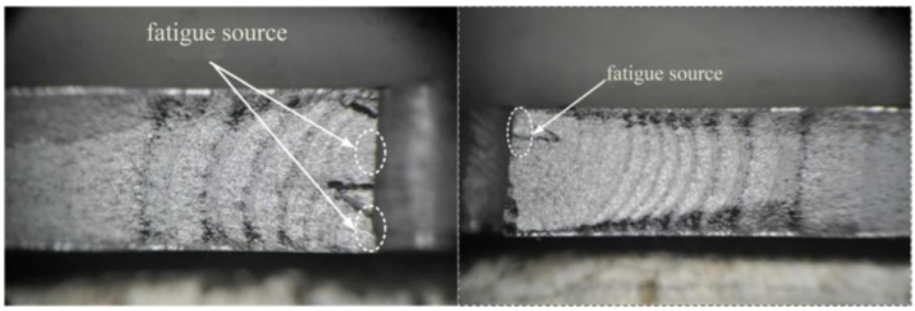

Fig. 20 Fracture analysis

Table 3 Comparison between the sensor's results and the analysis of fracture

Crack length (mm)	Analysis of fracture	Monitoring result	Error (%)	Average error	Standard deviation
Initiation (0.1)	25,300	27,800	9.88	4.61 %	0.0364
1	34,400	35,090	2.00		
2	36,980	36,100	2.37		
3	38,660	37,020	4.20		

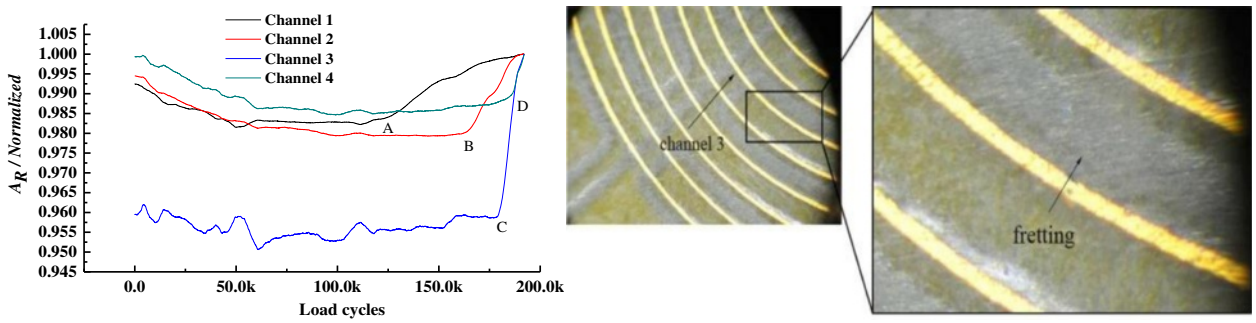

Fig. 21 Changes of signal sampled by the sensor (3 % NaCl + 10 % HNO_3 aqueous solution)

result that the load cycle intervals of four points decrease.

To validate the accuracy of the monitoring by the grating eddy current micro displacement sensor, a quantitative analysis of the fracture is accomplished with the PXS-5T microscope, as shown in Fig. 20. The comparison results are listed in Table 3. The results show that the error is less than 5 % except for initiation, which can be explained by the distance between first coil and the edge of sensor. Only if the crack extends more than 0.1 mm, will the sensing coil be able to monitor changes in the magnetic field.

In the second group, the sensor's performance in monitoring the corrosion fatigue crack is investigated. The experiment is carried out under an aggressive environment. The specimen and sensor are immersed in 3 % NaCl + 5 % HNO_3 aqueous solution contained in a plexiglass box. The conductivity of the corrosive solution is higher than the air's, and as a result, the distribution of inducing magnetic field is disturbed. The sampled signal is shown in Fig. 21. The amplitude of the third channel is markedly lower than the other, which may be because of wear of polyimide foil. Due to the fretting fatigue between the foil and the bolt, wear and tear occurs on the foil. The groove depth of the washer should be increased to protect the sensor, and we may carry further study in our succeeding works.

9 Conclusions

1. To monitor cracks in the metal structure of an aircraft, a kind of change-prone embedded grating eddy current array sensor is proposed, and a crack extension experiment aiming at verifying the performance of the sensor is carried out. The sensor is capable of measuring the crack with the accuracy of 1 mm, and the average error is 4.6 % compared with fracture analysis. A corrosive environment may affect the distribution of the magnetic field, but the purpose of the sensor serves detection successfully. With the help of the washer, the sensor is easy to integrate with the structure to be monitored and the load is transferred by the washer to protect the sensor.
2. By extracting the conductivity of the material as the crack feature, the semi-analytical equivalent model is established. The distributions of eddy current field and electromagnetic fields are explored. As the lift-off increases, the trans-impedance grids are all contracting towards to the load point which represents the sensor's output in the air. While at the frequency of 1 MHz, the sensitivity is largest in the middle range of conductivity. With the increase of frequency, the eddy current is concentrating on the surface of the structure which will reduce the capability of monitoring the deep cracks in the structure. Wear appears on the polyimide foils, and as a result, certain signals may decrease markedly.

Acknowledgements
The authors would like to thank the National High Technology Research and Development of China (2009AA04Z406).

Authors' contributions
SJ and HD designed the eddy current sensor and the smart washer. PL conducted the optimization of the sensor. XL and LC carried out the monitoring test. All authors read and approved the final manuscript.

Competing interests
The author had declared no competing interests in the manuscript.

Author details
[1]Aeronautic and Astronautic Engineering College, Air Force Engineering University, Xi'an 710038, China. [2]Co-Innovation Center for Advanced Aero-Engine, Beijing 710038, China. [3]School of Software, XiDian University, Xi'an 710038, China.

Received: 14 May 2016 Accepted: 9 August 2016
Published online: 18 August 2016

References

1. Y Shenfang, *Structural Health Monitoring and Damage Control* (National Defense Industry Press, Beijing, 2007)
2. CR Farrar, K Worden, An introduction to structural health monitoring. Philos. Trans. R. Soc. A Math. Phys. Eng. Sci. **365**(1851), 303–315 (2007)
3. JH Yin, HH Zhu, KW Fung et al., Innovative optical fiber sensors for monitoring displacement of geotechnical structures, in *Proceedings of the HKIE Geotechnical Division 28th Annual Seminar, Hong Kong*, 2008, pp. 287–294

4. M Majumder, TK Gangopadhyay, AK Chakraborty et al., Fiber Bragg gratings in structural health monitoring-present status and applications. Sensor Actuators A: Physical **147**(1), 150–164 (2008)
5. CH Tan, YG Shee, BK Yap et al., Fiber Bragg grating based sensing system: early corrosion detection for structural health monitoring. Sensors Actuators A Phys. **246**, 123–128 (2016)
6. G.W. Li, C.Y. Hong, J. Dai, et al. FBG-based creep analysis of GFRP materials embedded in concrete, mathematical problems in engineering, 2013(2013)
7. HF Pei, P Cui, JH Yin et al., Monitoring and warning of landslides and debris flows using an optical fiber sensor technology. J. Mt. Sci. **8**(5), 728–738 (2011)
8. W Lee, WJ Lee, SB Lee et al., Measurement of pile load transfer using the fiber bragg crating sensor system. Can. Geotech. J. **41**(6), 1222–1232 (2004)
9. XL Weng, JX Chen, J Wang, *Fiber Bragg Grating-Based Performance Monitoring of Piles Fiber in a Geotechnical Centrifugal Model Test. Advances in Materials Science and Engineering*, 2014
10. HJ Bassler, D Eifler, *Characterization of Plasticity Induced Martensite Formation During Fatigue of Austenitic Steel. Low-cycle Fatigue and Elasto-plastic Behavior of Materials*, 1998, pp. 235–240
11. RR Prairie, WJ Zimmer, *Statistical Modeling for Particle Impact Noise Detection Testing. Annual SYMP on Reliability and Maintainability*, 1991, pp. 536–540
12. G Yang, A Tamburrino, L Udpa, SS Udpa et al., Pulsed eddy-current based giant magnetoresistive system for the inspection of aircraft structures. IEEE Trans. Magn. **46**(3), 910–917 (2010)
13. NV Nair, VR Melapudi, HR Jimenez et al., AGMR-based eddy current system for NDE of aircraft structures. IEEE Trans. Magn. **42**(10), 910–917 (2006)
14. JS Knopp, JC Aldrin, KV Jata, Computational methods in eddy current crack detection at fastener sites in multilayer structures. Nondestructive Testing and Evaluation **24**(1–2), 103–120 (2009)
15. SS Udpa, PO Moore, *Nondestructive Testing Handbook. Electromagnetic Testing, American Society for Nondestructive Testing*, 2004
16. G Almeida, J Gonzalez, L Rosado, Advances in NDT and materials characterization by eddy currents. Procedia CIRP **7**, 359–364 (2013)
17. J Vishnuvardhan, A Muralidharan, CV Krishnamurthy et al., Structural health monitoring of anisotropic plates using ultrasonic guided wave STMR array patches. NDT&E International **42**(3), 193–198 (2009)
18. NJ Goldfine, D Clark, *Introduction to the Meandering Winding Magnetometer (MWM) and the Grid Measurement Approach. Conference on Nondestructive Evaluation of Materials and Composites, Scottsdale*, 1996, pp. 186–192
19. R Russell, D Jablonski, A Washabaugh et al., *Development of Meandering Winding Magnetometer Eddy Current Sensors for the Health Monitoring Modeling and Damage Detection of High Temperature Composite Materials* (32nd HIGH TEMPLE Workshop, Palm Springs, 2012)
20. RTCA DO-245A, *Minimum Aviation Systems Performance Standards for Local Area Augmentation System(LAAS)* (RTCA Inc, Washington DC, 2004)
21. R.A. Smith, G.R. Hugo, Deep corrosion and crack detection in aging aircraft using transient eddy-current NDE. The 5th Joint NASA/FAA/DOD Conference on Aging Aircraft, Orlando, Sept, 2001
22. RA Smith, GR Hugo, Transient eddy-current NDE for ageing aircraft-capabilities and limitations. Insight **43**(1), 14–20 (2001)
23. V Zilberstein, K Walrath, D Grundy et al., MWM eddy-current arrays for crack initiation and growth monitoring. Int. J. Fatigue **25**(9), 1147–1155 (2003)
24. V Zilberstein, D Grundy, V Weiss et al., Early detection and monitoring of fatigue in high strength steels with MWM-arrays. Int. J. Fatigue **27**(10), 1644–1652 (2005)
25. Y Sheiretov, D Grundy, V Zilberstein et al., MWM-array sensors for in situ monitoring of high-temperature components in power plants. Sensors **9**(11), 1527–1536 (2009)
26. Z Xu, H Zhang, V Sugumaran, K-KR Choo, L Mei, Y Zhu, Participatory sensing-based semantic and spatial analysis of urban emergency events using mobile social media. EURASIP J. Wirel. Commun. Netw. **2016**, 44 (2016)
27. Z. Xu, H. Zhang, C. Hu, L. Mei, J. Xuan, K.-K.R. Choo, V. Sugumaran, Y. Zhu, Building knowledge base of urban emergency events based on crowdsourcing of social media. Concurrency and Computation: Practice and Experience (2016). doi: http://dx.doi.org/10.1002/cpe.3780
28. Z. Xu, Y. Liu, N. Yen, L. Mei, X. Luo, X. Wei, C. Hu, Crowdsourcing based description of urban emergency events using social media big data. IEEE Transactions on Cloud Computing. doi: http://dx.doi.org/10.1109/TCC.2016.2517638
29. ZH Xiaojuan, K Guang-chang, X Junhua, Engineering application and analysis of HM109-1 sealant in helicopter. Journal of Helicopter Technique **165**(4), 52–55 (2010)
30. C Reboud, D Premel, D Lesselier et al., Recent advances in simulation of eddy current testing of tubes and experimental validations. Review of Progress in Quantitative Nondestructive Evaluation **26**, 241–248 (2007)
31. ZQ Lang, A Agurto, GY Tian et al., A system identification based approach for pulsed eddy current non-destructive evaluation. Journal of Measurement Science and Technology **18**(7), 2083–2091 (2007)
32. Y Nagaya, T Takagi, T Uchimoto et al., Identification of multiple cracks from eddy-current testing signals with noise sources by image processing and inverse analysis. Journal of IEEE Transactions on Magnetics **40**(2), I112–I1115 (2004)
33. DY Song, N Takeda, A Kitano, Correlation between mechanical damage behavior and electrical resistance change in CFRP composites as a health monitoring sensor. J. Mater. Sci. Eng. **456**, 286–291 (2007)
34. H Speckmann, *Structure Health Monitoring* (IMRBPB Meeting, Cologne, Germany, 2007)
35. FB Hildebrand, *Advanced Calculus for Applications* (Prentice Hall, Englewood Cliffs, 1962)